Microstructure simulation of rapidly solidified ASP30 high-speed steel particles by gas atomization

Jie Ma[1,2], *Bo Wang*[1,2], *Zhi-liang Yang*[1,2], *Guang-xin Wu*[1,2], *Jie-yu Zhang*[1,2], *and Shun-li Zhao*[3]

1) State Key Laboratory of Advanced Special Steel, Shanghai University, Shanghai 200072, China

2) School of Materials Science and Engineering, Shanghai University, Shanghai 200072, China

3) Research Institute, Baoshan Iron & Steel Co., Ltd., Shanghai 201900, China

Abstract: In this study, the microstructure evolution of rapidly solidified ASP30 high-speed steel particles was predicted using a simulation method based on the cellular automaton-finite element (CAFE) model. The dendritic growth kinetics, in view of the characteristics of ASP30 steel, were calculated and combined with macro heat transfer calculations by user-defined functions (UDFs) to simulate the microstructure of gas-atomized particles. The relationship among particle diameter, undercooling, and the convection heat transfer coefficient was also investigated to provide cooling conditions for simulations. The simulated results indicated that a columnar grain microstructure was observed in small particles, whereas an equiaxed microstructure was observed in large particles. In addition, the morphologies and microstructures of gas-atomized ASP30 steel particles were also investigated experimentally using scanning electron microscopy (SEM). The experimental results showed that four major types of microstructures were formed: dendritic, equiaxed, mixed, and multi-droplet microstructures. The simulated results and the available experimental data are in good agreement.

Keywords: high-speed steel; rapid solidification; microstructure; grain growth; gas atomization

1. Introduction

Gas atomization is an important rapid solidification technique with many advantages compared with traditional casting techniques. In the atomization process, the liquid is acted by gas and then broken into small droplets. These small droplets are subsequently solidified on a substrate to form the object in the desired shape. Particles produced by gas atomization exhibit excellent characteristics such as refined grains, reduced microsegregation, and extended solubility of alloying elements [1–2]. These characteristics are largely a consequence of the remarkable undercooling and cooling rate, which are, in turn, caused by the containerless solidification in the gas atomization chamber and the high velocity of the moving cold gas stream [3]. To date, numerous alloys with excellent characteristics have been produced by the gas atomization technique.

Because of the excellent characteristics of gas atomization, investigations of the solidification behaviors of gas-atomized alloy particles have attracted much attention [4–6]. Behúlová *et al.* [4] investigated the solidification microstructure of gas-atomized Ch12MF4 tool steel particles and reported that the transition from a dendritic to a cellular microstructure occurs via the mechanism of fragmentation of metastable austenite dendrites. Rokni *et al.* [5] demonstrated that the microstructure of rapidly solidified gas-atomized 7075 aluminum powder comprised two different particle types that were differentiated by their grain boundary structures and solute element distributions. Song *et al.* [6] investigated gas-atomized Fe–6.5wt%Si powders with different nucleation abilities and reported that the nucleation ability of the melt could influence the solidification microstructure of gas-atomized droplets. Although numerous experimental investigations have been conducted over the past several years, the temperature field and the solidification microstructure evolution in the rapid solidification process are very difficult to obtain experimentally in real industrial production environments because of the rapid ve-

🙎 Springer

locity of the droplets during the gas atomization process. Recently, great attention has been focused on using numerical simulations to predict the solidification behaviors of the droplets during atomization [7–9]. Tourret *et al.* [7] simulated the phase transformations of gas-atomized Al–Ni powders during solidification and observed that the phase fractions depend on particle size. Kusý *et al.* [8] investigated the thermal history of gas-atomized droplets with different diameters using the thermokinetic Newtonian model and reported that the nucleation temperature, recalescence temperature, and the duration of the quasi-isothermal plateau are the most important parameters that influence the microstructure development during gas atomization. Moreover, Xu *et al.* [9] used a numerical approach to analyze the heat transfer of an individual droplet.

Although previous research has provided valuable information about the temperature histories of droplets, no equivalent research into predicting the microstructure of gas-atomized particles has been reported. The ability to predict the microstructure of gas-atomized particles would be useful for achieving the final desired casting microstructure, which, because of the primary microstructure of the particle, could influence the final microstructure and the properties of alloy objects [10]. Thus, improvement of the predictive capability for gas-atomized alloy droplets' microstructures is necessary in industrial production.

In this study, to improve the predictive capability for the microstructure of rapid-solidified particles, we used a simulation method based on the cellular automaton–finite element (CAFE) model to predict the temperature fields and the microstructure evolution of rapidly solidified gas-atomized ASP30 high-speed steel particles. This high-alloy steels with high wear resistance can be used as tool materials because of the densification of rapidly solidified droplets, which is enhanced by the gas atomization technique [11]. The dendritic growth kinetics, in view of the characteristics of ASP30 high-speed steel, were calculated and used to simulate the microstructure of the particles. The effects of particle diameter on undercooling and on the convection heat transfer coefficient were then investigated to provide the cooling conditions for use in the microstructure simulation. Finally, the morphologies and microstructures of the particles were investigated experimentally.

2. Experimental procedure

ASP30 high-speed steel particles with a chemical composition of 1.28 C, 4.2 Cr, 5 Mo, 3.1 V, 6.4 W, 8.5 Co, 0.5 Mn, 0.5 Si, 0.01 P, 0.01 S, and balance Fe (wt%), manufac-

tured by nitrogen-gas atomization at a pressure of 2 MPa at 1717 K, were supplied by Baoshan Iron & Steel Co., Ltd., Shanghai, China. The particles with different diameters were mounted with epoxy and then polished to 0.5 μm. An etching solution of 5vol% HNO_3 in alcohol was used for the final cross-section microstructure examination. The morphologies and the microstructure of ASP30 high-speed steel particles were investigated using scanning electron microscopy (SEM) (JSM–6700F at an accelerating voltage of 10 kV).

3. Simulation methods

The CAFE model [12], combined with the finite element method (FEM) and the cellular automaton (CA) method, was used to simulate the microstructures of gas-atomized particles. The CAFE model includes a nucleation model and a dendritic growth model, which are described as follows.

3.1. Nucleation model

The nucleation model assembled within the CAFE model is a continuous nucleation model based on a Gaussian distribution [12]. It can be expressed as [13]

$$\frac{dn}{d(\Delta T)} = \frac{n_{max}}{\sqrt{2\pi}\Delta T_\sigma} \exp\left(-\frac{1}{2}\cdot\frac{\Delta T - \Delta T_{max}}{\Delta T_\sigma}\right) \tag{1}$$

where $dn/d(\Delta T)$ is a continuous nucleation distribution function, dn is the change in grain density, $d(\Delta T)$ is the increase of undercooling, ΔT_{max} is the mean undercooling, ΔT_σ is the standard deviation of undercooling, and n_{max} is the maximum density of nuclei.

3.2. Dendritic growth model

The dendritic growth model in the CAFE model, as implemented in the CALCOSOFT software, was developed by Kurz *et al.* [14]; it is referred to as the KGT model. The previously used KGT model is not suitable for rapid solidification processes because it disregards non-equilibrium effects in the rapid solidification process. Thus, in the present work, the model developed by Boettinger *et al.* [15], referred to as the BCT model, was used in place of the KGT model; user-defined functions (UDFs) were used to describe the dendritic growth in non-equilibrium rapid solidification processes.

In the BCT model, the total bulk undercooling ΔT of the dendrite tip is generally composed of four contributions [16]:

$$\Delta T = \Delta T_t + \Delta T_c + \Delta T_r + \Delta T_k \tag{2}$$

$$\Delta T_t = \frac{\Delta H}{c_{pL}} I_V(Pe_t) \tag{3}$$

$$\Delta T_{\mathrm{c}} = mc_0 \left[1 - \frac{m_{\mathrm{L}}'/m}{1-(1-k_{\mathrm{v}})I_{\mathrm{V}}(Pe_{\mathrm{c}})} \right] \qquad (4)$$

$$\Delta T_{\mathrm{r}} = \frac{2\Gamma}{R} \qquad (5)$$

$$\Delta T_{\mathrm{k}} = \frac{VR_{\mathrm{g}}T_{\mathrm{L}}^2}{\Delta HV_0} \qquad (6)$$

where ΔT_{t} is the thermal undercooling, ΔT_{c} is the solutal undercooling, ΔT_{r} is the curvature undercooling, ΔT_{k} is the kinetic undercooling, Γ is the Gibbs–Thomson coefficient, ΔH is the heat of fusion, $c_{p\mathrm{L}}$ is the specific heat, $Pe_{\mathrm{t}} = VR/2\alpha$ and $Pe_{\mathrm{c}} = VR/2D$ are the thermal and solutal Péclet numbers, respectively, α is the thermal diffusivity, and D is the chemical diffusion coefficient. Parameter $I_{\mathrm{V}}(Pe_{\mathrm{t}})$ is the solutal Ivantsov function of thermal Péclet number, $I_{\mathrm{V}}(Pe_{\mathrm{c}})$ is the solutal Ivantsov function of solutal Péclet number, m is the liquidus slope, m_{L}' is the actual liquidus slope under non-equilibrium conditions, c_0 is the nominal alloy composition, V_0 is the velocity of sound as an upper limit for the solidification velocity, R_{g} is the gas constant, and k_{v} is the actual solute partition coefficient.

In the microstructure simulation process, consideration of the relationship between growth velocity and undercooling is necessary because it can reflect the dendritic growth kinetics. Eq. (2) shows the relationship among dendritic growth velocity, dendrite radius, and undercooling. However, the relationship between dendritic growth velocity and undercooling cannot be expressed well using only Eq. (2); therefore, the following equation was adopted to describe the dendrite radius and growth velocity according to the solvability theory [17–19]:

$$R = \frac{\Gamma/\sigma^*}{\dfrac{\Delta H}{c_{p\mathrm{L}}}Pe_{\mathrm{t}}\xi_{\mathrm{t}} - \dfrac{2m_{\mathrm{L}}'c_0(1-k)Pe_{\mathrm{t}}\xi_{\mathrm{t}}}{1-(1-k_{\mathrm{v}})I_{\mathrm{V}}(Pe_{\mathrm{c}})}} \qquad (7)$$

where

$$\xi_{\mathrm{t}} = 1 - \frac{1}{1+\sqrt{1+\dfrac{1}{\sigma^* Pe_{\mathrm{t}}^2}}} \qquad (8)$$

$$\xi_{\mathrm{c}} = 1 + \frac{2k}{1-2k-\sqrt{1+\dfrac{1}{\sigma^* Pe_{\mathrm{c}}^2}}} \qquad (9)$$

Here, σ^* is the stability constant, k is the solute partition coefficient, and ξ_{t} and ξ_{c} are the thermal and solutal stability functions, respectively. The analytical solutions are difficult to obtain though complex Eqs. (2)–(9). Consequently, numerical solutions of the BCT model were obtained by mathematical treatment in present work. First, we defined parameters $f(R,V)$ and $F(R,V)$ expressed in Eq. (7) by Eqs.

(10)–(11):

$$f(R,V) = \frac{\Delta H}{c_{p\mathrm{L}}}Pe_{\mathrm{t}}\xi_{\mathrm{t}} - \frac{2m_{\mathrm{L}}'c_0(1-k)Pe_{\mathrm{c}}\xi_{\mathrm{c}}}{1-(1-k_{\mathrm{v}})I_{\mathrm{V}}(Pe_{\mathrm{t}})} \qquad (10)$$

$$F(R,V) = \frac{\Gamma}{\sigma^*} - Rf(R,V) \qquad (11)$$

The available values of V and R were then obtained through Eqs. (2)–(11) with the values of $F(R,V)$ set as zero. Finally, the values of ΔT were obtained through Eq. (2) using the previously obtained values for V and R as inputs.

Usually, these series of values (i.e., ΔT, V, and R) are obtained by program calculations and are subsequently used to be fitted by initial certain curves. Previous studies have shown that three major types of fitting equations can be used to describe the relationship between V and ΔT [20–22], as shown in Eqs. (12)–(14), where Eq. (15) is introduced as an extension of Eq. (14):

$$V = a\Delta T^b \qquad (12)$$

$$V = a\,\mathrm{e}^{b\Delta T} \qquad (13)$$

$$V = a\Delta T + b\Delta T^2 \qquad (14)$$

$$V = a\Delta T + b\Delta T^2 + c\Delta T^3 \qquad (15)$$

In the present work, Eqs. (12)–(15) were used to fit the obtained series of values (ΔT, V, and R).

4. Simulation results and discussion

With respect to the microstructure simulation of ASP30 high-speed steel particles, three main steps are involved. First, the mathematical relationship between dendrite growth velocity and undercooling must be solved. For this purpose, we developed a mathematical treatment for the BCT model in the present work. Second, good knowledge of the different cooling conditions and undercooling in particles with different diameters should be obtained before starting the simulation process. In model terms, this step involves calculation of the mathematical relationship among the particle diameter, undercooling, and the convection heat transfer coefficient. Third, the temperature field of particles, which is another important input item for the final microstructure simulation, should be calculated using the two previously established mathematical relationships. The details related to these three steps in the present simulation process are described as follows.

The thermophysical ASP30 high-speed steel parameters used for the calculation of the mathematical relationship between dendrite growth velocity and undercooling are listed in Table 1. The calculated results and fitting curves are shown in Fig. 1. Figs. 1(a)–1(d) reveal that Eqs. (12) and (15) provide better curve-fitting results than Eqs. (13) and

(14). However, because the final result calculated using Eq. (15) included negative parameters, which is not beneficial for the convergence of the simulation, we selected Eq. (12) as the most appropriate fitting equation in the present work. As shown in Fig. 1(a), the dendritic growth velocity obviously increases with the increasing of undercooling. The power-function relationship shown in Eq. (16) was obtained in the present work:

$$V = 2.46 \times 10^{-6} \Delta T^{2.95} \tag{16}$$

Thus, the dendritic growth velocity V can be attained for a given value of undercooling ΔT by solving Eq. (16). Notably, this relationship is a significant criterion for simulating the solidification microstructure in the rapid solidification process.

Table 1.   Thermophysical parameters of ASP30 high-speed steel

Liquidus temperature, T_L / (K)	1617
Specific heat, c_{pL} / (J·kg^{-1}·K^{-1})	600
Density of particles, ρ_d / (kg·m^{-3})	7332
Heat of fusion, ΔH / (J·kg^{-1})	4.7×10^5
Interface energy, σ_{SL} / (J·m^{-2})	0.331
Thermal diffusion coefficient, α / (m^2·s^{-1})	7×10^6
Gibbs–Thomson coefficient, Γ / (K·m)	3×10^7
Characteristic diffusion length, a_0 / (m)	2.5×10^9
Diffusion coefficient, D / (m^2·s^{-1})	8×10^9
Speed of sound, V_s / (m·s^{-1})	2000
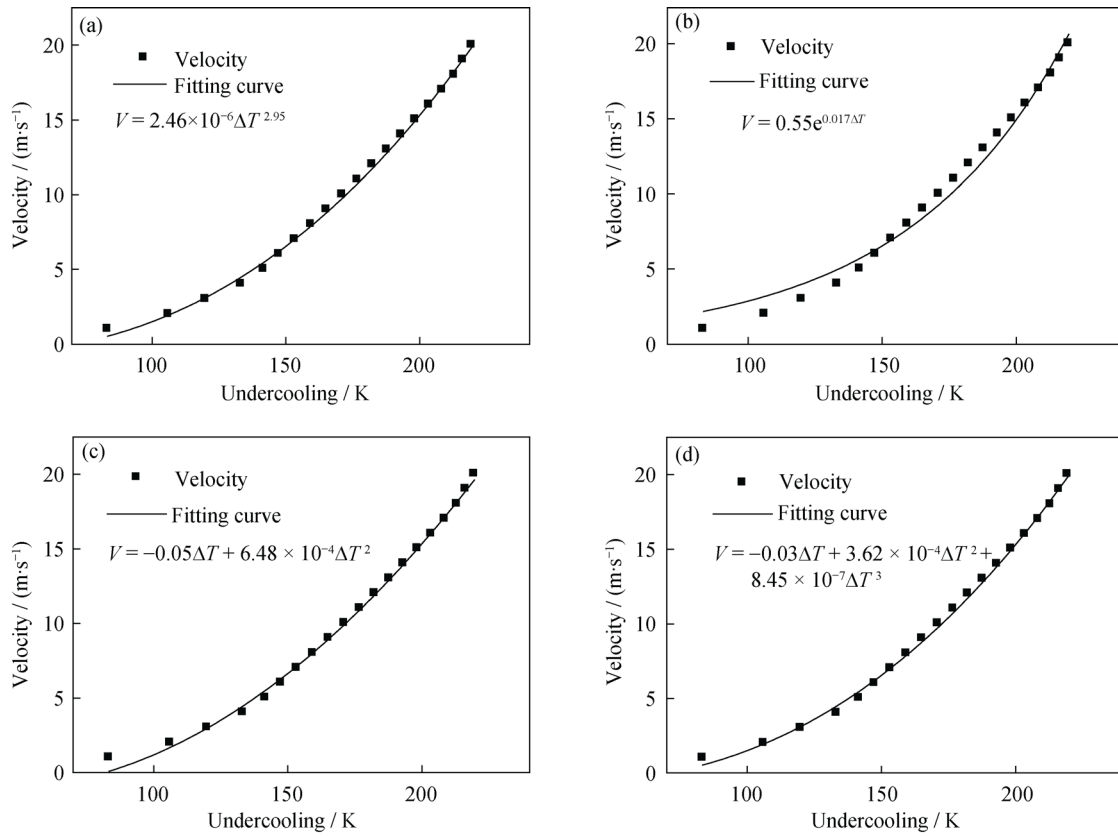
Fig. 1.   Relationships between dendritic growth velocity and undercooling.

In the gas atomization process, droplets with different diameters experience different cooling conditions and different undercooling. Therefore, the convection heat transfer coefficient h and the undercooling ΔT of different particle diameter D_i should be calculated before the microstructure simulation. According to the work of Lee and Ann [23], h, ΔT, and D_i can be calculated using Eqs. (17)–(23):

$$h = \frac{k_g}{D_i}(2.0 + 0.6\sqrt{Re}\sqrt{P_r}) \tag{17}$$

$$Re = \rho_g D_i \mu_g^{-1} |u_d - \mu_g| \tag{18}$$

$$u_d = \frac{u_0(T_N - T_g)}{T_m} \tag{19}$$

$$Pr = \frac{c_{pg}\mu_g}{k_g} \tag{20}$$

$$\frac{\Psi}{T_N \Delta T} = \ln\left[\frac{\frac{\pi}{6}K_v\rho_d c_{pL}T_N^2 D_i^4}{6h\Psi(3T_N - T_L)(T_N - T_g)}\right] \tag{21}$$

$$\Psi = \frac{16\pi\sigma_{SL}^3 T_L^2 f(\theta)}{3k_B\rho_d^2 \Delta H^2} \tag{22}$$

298

Int. J. Miner. Metall. Mater., Vol. 23, No. 3, Mar. 2016

$$f(\theta) = \frac{2 - 3\cos\theta + \cos^3\theta}{4} = a_2 + \frac{a_3}{D_i} \qquad (23)$$

where k_g is the thermal conductivity of the gas; Re is the Reynolds number; Pr is the Prandtl number of the gas; ρ_d is the density of the particles; u_d is the axial velocity of the alloy droplet; u_g is the dynamic viscosity of the gas; u_0 is the initial exit axial velocity of the gas, with a value $u_0 = 200$ m·s^{-1} [24]; T_N, T_g, and T_L are the temperatures of nucleation, gas, and liquidus, respectively; c_{pg} is the specific heat of the gas, K_v is a kinetic parameter with a value of 10^{40} m^{-3}·s^{-1}; k_B is the Boltzmann constant; σ_{SL} is the solid–liquid interface energy; and $f(\theta)$ is the catalytic efficiency for heterogeneous nucleation. In the present work, two typical values of $f(\theta) = 0$ for 1200 μm diameter particles [25] and $f(\theta) = 1$ for 1 μm diameter particles [26] were set to receive the constant values of $a_2 = -8.34 \times 10^{-4}$ and $a_3 = 1.0008$, respectively.

The thermophysical parameters of nitrogen used for cooling condition calculations are listed in Table 2 [9]. The values of h and ΔT calculated using Eqs. (17)–(23) are summarized in Table 3 and Fig. 2. In the present work, the particle diameter sizes range from 20 μm to 100 μm and the pouring temperature is 1717 K. As evident in Fig. 2, both the convection heat transfer coefficient and the undercooling increase with decreasing particle diameter. The calculated values listed in Table 3 were used as inputs in the final microstructure simulations.

Table 2.   Thermophysical parameters of N$_2$

Specific heat, c_{pg} / (J·kg^{-1}·K^{-1})	Dynamic viscosity, μ_g / (N·s·m^{-2})	Thermal conductivity, k_g / (W·m^{-1}·K^{-1})	Density, ρ_g / (kg·m^{-3})
1039	1.78×10^{-5}	2.6×10^{-2}	1.16

Table 3.   Calculated results of undercooling and convection heat transfer coefficient for ASP30 high-speed steel particles under an N$_2$ atmosphere

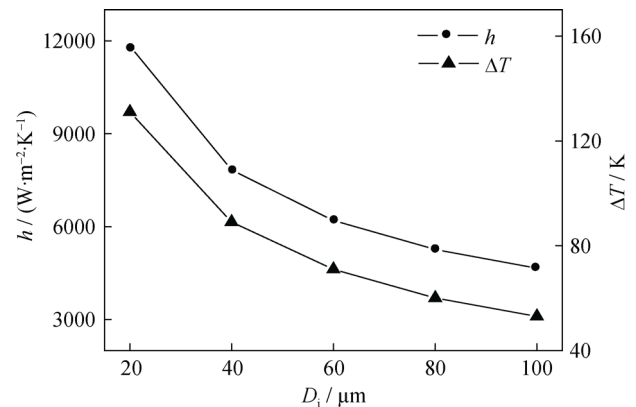| Particle diameter / μm	Convection heat transfer coefficient / (W·m^{-2}·K^{-1})	Undercooling / K
20	11832	131
40	7828	89
60	6179	71
80	5266	60
100	4649	53

As previously mentioned, the temperature field is another important variable for the final microstructure simulation. In the solidification process, the temperature T can reflect the undercooling ΔT according to the relationship

$$\Delta T = T_L - T \qquad (24)$$

where ΔT can be obtained for a given value of T. The den-

dritic growth velocity V can then be calculated though Eq. (16) using ΔT as inputs. The calculated values of V can then be used to simulate the final microstructure.

Fig. 3 presents the temperature fields in cross-sections of particles with different diameters at a simulation time of 0.0004 s. Temperature difference is presented with different colors. Apparently, the temperature gradient in ASP30 steel particles can be ignored in a rapid solidification gas-atomization process. As shown in Fig. 3, the temperature at the particle surface is lower than that at the particle center. This phenomenon indicates that gas-atomized particles cooled from their exterior to their interior. In addition, the particle's temperature simultaneously decreased with decreasing diameter, primarily as a consequence of the high cooling rate that resulted from the large convection heat transfer coefficient of the small particle (see Fig. 2).


Fig. 2.   Effects of particle diameter on the convection heat transfer coefficient and undercooling.

The simulation parameters used in the present microstructure simulations are listed in Table 4. Fig. 4 shows the simulated cross-section microstructures of ASP30 high-speed steel particles with different particle diameters. In Fig. 4, different grain orientations are indicated with different colors. As evident in this figure, the microstructures of the particles clearly vary with the particle diameter. Refined equiaxed grains dominate the particles with diameters of 100 μm and 80 μm. In the case of the 60 μm particle, a thin columnar zone appeared at the surface and the remainder was filled with equiaxed grains. As shown in Fig. 4(b), equiaxed grains formed only in the center of the 40 μm particle. Notably, however, very limited equiaxed grains were observed in the center of the 20 μm particle. The transgranular columnar microstructure was observed in the whole cross-section of the 20 μm particle. Similar microstructures were reported by Behulova *et al.* [27], who observed that the columnar dendritic microstructure appeared predominantly in large Ch12MF4 steel particles, whereas equiaxed and

fragmented dendritic microstructures occurred in smaller particles during gas atomization. These results are attributable to the size reduction, which leads to an increase of undercooling (see Fig. 2) and a decrease in bulk nucleation. These results are similar to previously reported results that indicate nucleation often occurs at the surfaces of very fine particles [28]. In addition, because of the reduction of the particle diameter, the increase in the convection heat transfer coefficient and in the cooling rate (see Fig. 2) lead an increase of the dendritic growth velocity. The existing nuclei in the surface grow rapidly ahead of the liquid zone along the inverse direction of heat flow. Thus, the large convection heat transfer coefficient and the large undercooling lead to the appearance of the final columnar zone. Conversely, the small convection heat transfer coefficient and the small undercooling in large particles results in a low growth velocity of dendrites and in extensive bulk nucleation. These nuclei restrict the growth of columnar grains in the surface and result in the final equiaxed microstructure. Therefore, the dendritic microstructure is usually observed in small particles, whereas the grain-refined equiaxed microstructure is always observed in large particles.
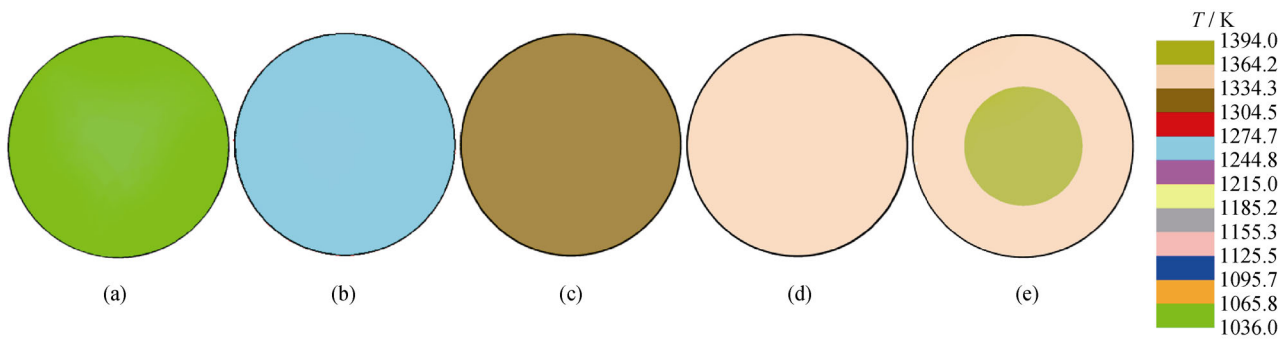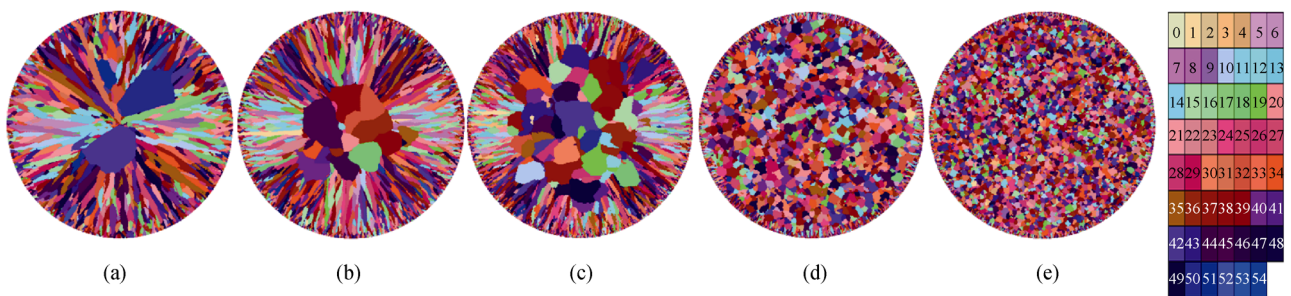

Fig. 3. Simulated temperature fields at 0.0004 s with different diameters: (a) 20 μm, (b) 40 μm, (c) 60 μm, (d) 80 μm, and (e) 100 μm.

Table 4. Parameters used in the microstructure simulation

Droplet diameter / μm	Pouring temperature / K	$n_{max,s}$ / m^{-2}	$n_{max,v}$ / m^{-2}	$\Delta T_{\sigma,v}$ / K	$\Delta T_{\sigma,s}$ / K
20–100	1717	2×10^{13}	8×10^{19}	5	0.1

Note: $n_{max,s}$ —the maximum density of surface nuclei; $n_{max,v}$ —the maximum density of bulk nuclei; $\Delta T_{\sigma,s}$ —the standard deviation of surface undercooling; $\Delta T_{\sigma,v}$ —the standard deviation of bulk undercooling.

Fig. 4. Simulated microstructures of ASP30 steel particles with different diameters: (a) 20 μm, (b) 40 μm, (c) 60 μm, (d) 80 μm, and (e) 100 μm.

5. Results and discussion

ASP30 high-speed steel particles were manufactured by nitrogen gas atomization according to the simulation conditions. The process parameters used in the present experiments were the same as those used in the simulations. The morphologies and microstructures of gas-atomized particles were investigated experimentally using scanning electron microscopy (SEM).

5.1. Morphologies

The secondary electron (SE) images in Fig. 5 shows the morphologies of the gas-atomized ASP30 high-speed steel particles. These images reveal that the ASP30 high-speed steel particles are spherical or near-spherical in shape. However, a few small particles, typically 10–20 μm in diameter, were observed around the larger particles. Similar

small satellite particles were also observed in gas-atomized SAC305 particles by Wisutmethangoon *et al.* [29]. They may originate from the presence of turbulent flow in the atomization chamber, which results in collisions among droplets. The small droplets solidify rapidly and collide with the larger droplets that have not solidified completely, thereby becoming satellite particles of larger particles.
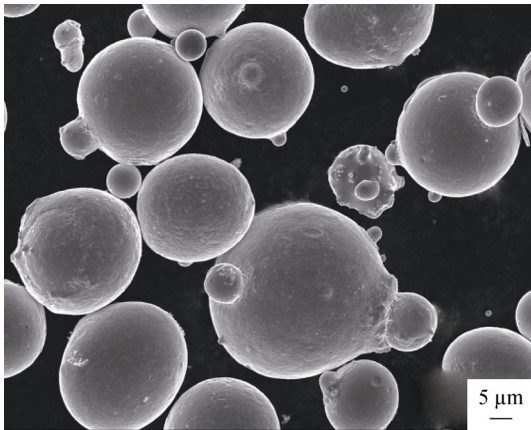

Fig. 5.   Morphologies of gas-atomized ASP30 high-speed steel particles.

5.2. Cross-section microstructures

Fig. 6 shows SEM images of cross-sections of ASP30 steel particles with different diameters. As evident in Figs. 6(a)–6(f), particles with different diameters exhibit different microstructures: columnar dendritic, grain-refined equiaxed, mixed microstructure (i.e., a mixture of equiaxed grains and the dendrite fragments), and multi-droplet microstructures. Behulova *et al.* [27] also observed dendritic, grain-refined, and compound (mixture of dendritic and grain-refined) microstructures in rapidly solidified particles. However, the multi-droplet microstructure, as shown in Figs. 6(e)–6(f), was not reported by Behulova *et al.* [27]. The formation of the multi-droplet microstructure is due to the collision phenomenon of droplets caused by turbulent flow in the atomization chamber. This collision phenomenon was confirmed by the morphological investigation of particles, as shown in Fig. 5. The small particles collide with the incompletely solidified large droplets and become new nuclei of the large particles. These new nuclei (see Figs. 6(e)–6(f)) grow rapidly and finally form the multi-droplet microstructure. Notably, multi-droplets are not considered in the present simulation work because of their specificity.

Fig. 6(a) shows the microstructure of a 25 μm particle. The major microstructure is columnar dendritic grains, which grow from the particle surface to the center, except for an equiaxed grain that appears in the particle center.

Moreover, SEM images of the cross-section of a 58 μm particle are shown in Fig. 6(b). A mixed microstructure (i.e., a mixture of equiaxed grains and dendrite fragments) was observed in most of the particle's center, whereas elongated columnar grains were observed at the particle surface. Fig. 6(c) and Fig. 6(d) show the microstructures of 80 μm and 102 μm particles, respectively. These figures indicate that both of the particles exhibit grain-refined equiaxed microstructures. These results are in a good agreement with the simulated results shown in Fig. 4. These results are explained by a reduction of the number of bulk nuclei as a consequence of the increase of undercooling (see Fig. 2) due to the reduction of the particle diameter. Thus, the nucleation occurs mostly at the surface of the particle. These nuclei at the particle surface grow rapidly toward the particle center, leading to the final elongated columnar dendritic microstructure. In addition, the increasing convection heat transfer coefficient (see Fig. 2) leads to an increase of the cooling rate, causing the formation of the final columnar microstructure. Thus, the large undercooling and the large convection heat transfer coefficient are the two important causes of the formation of the columnar dendritic microstructure. By contrast, in large particles, because of the small convection heat transfer coefficient and the release of latent heat, the melt temperature increases, leading to dendrite fragmentation. The liquid/solid interface becomes locally unstable. The fragmented dendrites in droplets form as new nuclei (see Figs. 6(e)–6(f)), growing and restricting the growth of columnar grains, and finally form the equiaxed microstructure. Furthermore, with increasing particle diameter, the increasing fragmented dendrites cause the large particle hard to achieve large undercooling. Cochrane *et al.* [30] have confirmed that large undercooling is difficult to achieve in large particles. The small undercooling in large particles results in the low dendritic growth velocity and then leads to the final equiaxed microstructure. Zambon *et al.* [31] have shown that dendritic structures are most frequently formed in the smallest particles, whereas equiaxed grains structure exhibit the opposite trend. Their results are similar to those reported here. A comparison of the experimental results in Fig. 6 with the simulation results in Fig. 4 reveals that the experimental results are in a good agreement with the simulated results. Therefore, on the basis of such a comparison of previously reported and the present experimental results, we conclude that the simulation method presented herein provides an effective method to predict the microstructure evolution during the gas atomization process.
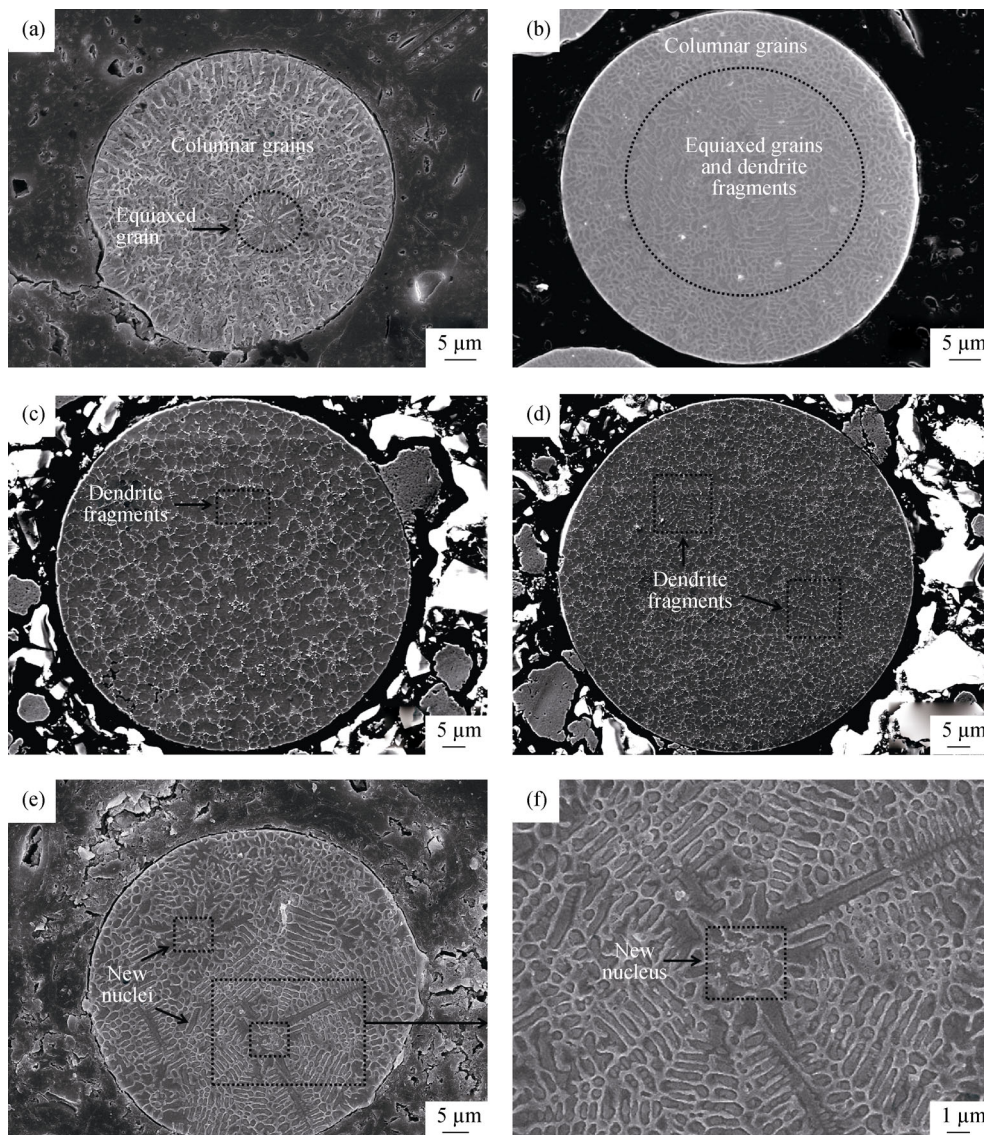
Fig. 6. **SEM micrographs of particles with different diameters: (a) 25 μm, (b) 58 μm, (c) 80 μm, (d) 102 μm, and (e) and (f) multi-droplet.**

6. Conclusions

The microstructure evolution of rapidly solidified gas-atomized ASP30 high-speed steel particles was investigated in the present work. The following important conclusions were drawn from the present work:

(1) The convection heat transfer coefficient and the undercooling are influenced by the diameter of the particles. Small particles have large convection heat transfer coefficients and large undercooling.

(2) Four major types of solidification microstructures were identified in the rapidly solidified ASP30 high-speed steel particles. They are dendritic microstructure, equiaxed microstructure, mixed microstructure, and multi-droplet microstructure.

(3) The simulation results reveal that the microstructures of gas-atomized ASP30 high-speed steel particles depend on the particle diameter. The predicted microstructures show that the columnar dendritic microstructure is usually observed in small particles, whereas the grain-refined equiaxed microstructure is observed in large particles during the gas atomization process. The simulated results were verified experimentally.

(4) The BCT dendritic growth model was successfully applied to predict the microstructures of gas-atomized ASP30 high-speed steel particles. The simulation results agree well with the experimental results, which provide a theoretical basis to investigate the microstructure evolution in the gas atomization process.

Acknowledgements

References

[1] A. García-Escorial and M. Lieblich, Microstructural characterisation of $Ni_{75}Al_{25}$ and $Ni_{31.5}Al_{68.5}$ powder particles produced by gas atomisation, *J. Alloys Compd.*, 586(2014), No. S1, p. S489.

[2] M. Yang, C.J. Song, Y.X. Dai, L. Zhu, K.F. Li, and Q.J. Zhai, Microstructural evolution of gas atomized Fe25Cr3.2C alloy powders, *J. Iron Steel Res. Int.*, 18(2011), No. 2, p. 75.

[3] C.J. Song, Y.Y. Guo, L. Zhu, K.F. Li, M. Yang, and Q.J. Zhai, Structure evolution of the atomized powders of Fe–25Cr–3.9C alloy with addition of ni and b elements, *Adv. Mater. Res.*, 239-242(2011), p. 44.

[4] M. Behúlová, J. Mesárošová, and P. Grgač, Analysis of the influence of the gas velocity, particle size and nucleation temperature on the thermal history and microstructure development in the tool steel during atomization, *J. Alloys Compd.*, 615(2014), Suppl. 1, p. S217.

[5] M.R. Rokni, C.A. Widener, and G.A. Crawford, Microstructural evolution of 7075 Al gas atomized powder and high-pressure cold sprayed deposition, *Surf. Coat. Technol.*, 251(2014), p. 254.

[6] C.J. Song, K.F. Li, K. Xie, W. Lu, S.C. Zhao, Q.Y. Han, and Q.J. Zhai, The effect of the nucleation ability on solidified microstructures of gas-atomized Fe–6.5 wt.%Si alloy powder, *Powder Technol.*, 263(2014), p. 31.

[7] D. Tourret, G. Reinhart, C.A. Gandin, G.N. Iles, U. Dahlborg, M. Calvo-Dahlborg, and C.M. Bao, Gas atomization of Al–Ni powders: solidification modeling and neutron diffraction analysis, *Acta Mater.*, 59(2011), No. 17, p. 6658.

[8] M. Kusý, M. Behulova, and P. Grgac, Influence of the thermal history of a particle during atomization on the morphology of carbides in a hypereutectic iron based alloy, *J. Alloys Compd.*, 536(2012), p. S541.

[9] Q. Xu and E.J. Lavernia, Influence of nucleation and growth phenomena on microstructural evolution during droplet-based deposition, *Acta Mater.*, 49(2001), No. 18, p. 3849.

[10] A.F. Norman, K. Eckler, A. Zambon, F. Gärtner, S.A. Moir, E. Ramous, D.M. Herlach, and A.L. Greer, Application of microstructure-selection maps to droplet solidification: a case study of the Ni–Cu system, *Acta Mater.*, 46(1998), No. 10, p. 3355.

[11] A. Fedrizzi, M. Pellizzari, and M. Zadra, Influence of particle size ratio on densification behaviour of AISI H13/AISI M3:2 powder mixture, *Powder Technol.*, 228(2012), p. 435.

[12] C.A. Gandin and M. Rappaz, A coupled finite element–cellular automaton model for the prediction of dendritic grain structures in solidification processes, *Acta Metall. Mater.*, 42(1994), No. 7, p. 2233.

[13] M. Rappaz and C.A. Gandin, Probabilistic modelling of microstructure formation in solidification processes, *Acta Metall.*

Mater., 41(1993), No. 2, p. 345.

[14] W. Kurz, B. Giovanola, and R. Trivedi, Theory of microstructural development during rapid solidification, *Acta Mater.*, 34(1986), No. 5, p. 823.

[15] W. Boettinger, S. Coriell, and R. Trivedi, *Rapid Solidification Processing*: *Principles and Technologies IV*, Edited by R. Mehrabian and P. Parrish, Claitor's Pub, Baton Rouge, LA, 1988, p. 13.

[16] X.R. Liu, C.D. Cao, and B. Wei, Microstructure evolution and solidification kinetics of undercooled Co–Ge eutectic alloys, *Scripta Mater.*, 46(2002), No. 1, p. 13.

[17] P.K. Galenko and M.D. Krivilyov, Modeling of a transition to diffusionless dendritic growth in rapid solidification of a binary alloy, *Comput. Mater. Sci.*, 45(2009), No. 4, p. 972.

[18] A.M. Mullis, Prediction of the operating point of dendrites growing under coupled thermosolutal control at high growth velocity, *Phys. Rev. E*, 83(2011), art. No. 061601.

[19] N. Liu, F. Liu, G.C. Yang, Y.Z. Chen, C.L. Yang, J.S. Li, and Y.H. Zhou, Dendrite growth in undercooled Fe–Co melt, *J. Alloys Compd.*, 455(2008), No. 1–2, p. L6.

[20] C. Panofen and D.M. Herlach, Solidification of highly undercooled Si and Si–Ge melts, *Mater. Sci. Eng. A*, 449–451(2007), p. 699.

[21] Y. Ruan and F.P. Dai, Rapid dendrite growth subjected to multi-solute trapping in an undercooled Fe-based quaternary alloy, *Intermetallics*, 25(2012), p. 80.

[22] Ph. Thévoz, J.L. Desbiolles, and M. Rappaz, Modeling of equiaxed microstructure formation in casting, *Metall. Trans. A*, 20(1989), No. 2, p. 311.

[23] E.S. Lee and S. Ahn, Solidification progress and heat transfer analysis of gas-atomized alloy droplets during spray forming, *Acta Mater.*, 42(1994), No. 9, p. 3231.

[24] W.B. Guan, Y.L. Gao, Q.J. Zhai, and K.D. Xu, Effect of droplet size on nucleation undercooling of molten metals, *J. Mater. Sci.*, 39(2004), No. 14, p. 4633.

[25] P. Mathur, D. Apelian, and A. Lawley, Analysis of the spray deposition process, *Acta Mater.*, 37(1989), No. 2, p. 429.

[26] C.G. Levi and R. Mehrabian, Heat flow during rapid solidification of undercooled metal droplets, *Metall. Trans. A*, 13(1982), No. 2, p. 221.

[27] M. Behulova, R. Moravcik, M. Kusy, L. Čaplovič, P. Grgac, and L. Stancek, Influence of atomisation on solidification microstructures in the rapidly solidified powder of the Cr–Mo–V tool steel, *Mater. Sci. Eng. A*, 304(2001), No. 1, p. 540.

[28] R. Trivedi, F. Jin, and I.E. Anderson, Dynamical evolution of microstructure in finely atomized droplets of Al–Si alloys, *Acta Mater.*, 51(2003), No. 2, p. 289.

[29] S. Wisutmethangoon, T. Plookphol, and P. Sungkhaphaitoon, Production of SAC305 powder by ultrasonic atomization, *Powder Technol.*, 209(2011), No. 1-3, p. 105.

[30] R.F. Cochrane, P.V. Evans, and A.L. Greer, Competitive growth analysis of phase formation in Al–8wt.% Fe, *Mater. Sci. Eng. A*, 133(1991), p. 803.

[31] A. Zambon, B. Badan, G. Vedovato, and E. Ramous, Morphologies in gas-atomized $Fe_{50}Ni_{30}Si_{10}B_{10}$ amorphizable alloy powders, *Mater. Sci. Eng. A*, 304-306(2001), p. 452.